

USING OPTIMIZED ECCENTRICITY REXOLITE LENS FOR ELECTRICAL BEAM STEERING WITH INTEGRATED APERTURE COUPLED PATCH ARRAY

A. Karttunen^{1, *}, J. Säily², A. E. I. Lamminen²,
J. Ala-Laurinaho¹, R. Sauleau³, and A. V. Räsänen¹

¹ Department of Radio Science and Engineering, SMARAD/MilliLab, School of Electrical Engineering, Aalto University, P. O. Box 13000, FI-00076 AALTO, Finland

²VTT Technical Research Centre of Finland, 02044 VTT, Finland

³Institute of Electronics and Telecommunications of Rennes (IETR), UMR CNRS 6164, University of Rennes 1, Rennes 35042, France

Abstract—Design and measurement results of a beam-steering integrated lens antenna at 77 GHz are presented. An 8-element LTCC aperture coupled patch antenna feed array with a switching network is used to electrically steer the main beam in H -plane. A 100-mm diameter Rexolite ($\epsilon_r = 2.53$) lens is simulated and tested. The eccentricity of the lens is optimized in an earlier work with ray-tracing simulations for improved beam-steering properties compared to the conventional extended hemispherical and elliptical lenses. The beam-steering properties including scan loss, main-beam width and direction, side-lobe levels, directivity, and cross-polarization are analyzed in detail with both simulations and radiation pattern measurements. As expected, the results show that the side-lobe and cross-polarization levels are not predicted accurately with large feed offsets using the ray-tracing simulations. Nevertheless, it is shown that the lens shape can be successfully optimized with the simple and fast ray-tracing simulations. The measured half-power beam-width at 77 GHz is $2.5^\circ \pm 0.2^\circ$ up to the largest tested beam-steering angle of 30° . The optimized eccentricity low permittivity lens results in smaller scan loss than the conventional lenses.

Received 29 August 2012, Accepted 21 September 2012, Scheduled 1 October 2012

* Corresponding author: Aki Karttunen (aki.karttunen@aalto.fi).

1. INTRODUCTION

Electrical beam steering with a narrow high-directivity beam has potential use in many millimeter-wave applications, such as automotive radar at 77–81 GHz with high angular resolution [1] or telecommunications for high data rate links at E-band (71–86 GHz) [2, 3]. One potential antenna solution is an integrated lens antenna with a feed array and switching network [3, 4]. The switches are used to select one of the feed array elements, and the lens produces the main beam in a direction relative to the active element's position on the lens bottom.

The conventional integrated lens types that produce diffraction-limited beams are the extended hemispherical lenses [3–11] and the elliptical ones [6, 8, 12–18]. The beam-steering properties have been widely studied with simulations [3–9, 12, 13], and with measurements without electrical beam steering, i.e., without switches, e.g., in [3, 5, 9, 12]. Moreover, double-shell integrated lenses [19, 20], and shaped integrated lens antennas with optimized lens shapes have been studied, e.g., in [13, 14]. The planar feed array is integrated to the flat surface of the lens, and the lens enhances the directivity of the relatively low-directivity feed array antenna element. As the feed is integrated into direct contact with the lens, it offers mechanical rigidity, elimination of substrate modes, and good coupling to the lens.

With a conventional elliptical lens, with an eccentricity of $(\epsilon_r)^{-1/2}$ and with the feed at the focal point, the rays emitted from the hemiellipse are parallel, and the equiphase surface is planar providing the diffraction-limited beam (see Fig. 7(i)). The directivity of an extended hemispherical lens can be optimized by selecting the extension length [3–5, 7–11]. Using a shorter extension leads to lower losses (e.g., [12]), but does not produce the diffraction-limited beam, and thus it is not preferable when narrow beam and high directivity are priority. With small beam-steering angles up to about 15°–25°, the elliptical lens is better, but with larger angles the extended hemispherical lens provides higher directivity and nearly constant beam width [6, 8]. With high permittivity lens, the difference between the elliptical and extended hemispherical lenses is relatively small [6], but with low permittivity lenses the differences in beam-steering properties are significant. In [8], an optimized eccentricity low permittivity integrated lens is investigated that combines the advantages of the conventional lenses: high directivity and constant beam width over a wide beam-steering range of $\pm 30^\circ$. In this paper, the promising theoretical results from [8] are tested in practice and analyzed in detail.

Electrical beam steering with integrated lens antenna requires both an array of feed elements and a switching network. The feed antennas, the switches, and other needed components can be integrated in one package using low-temperature cofired ceramic (LTCC) technology, e.g., [3, 21–28]. The LTCC packaging and integrated circuits are widely used at 60 GHz, e.g., [21–24]. LTCC has been used at W-band 77–110 GHz [3, 25–27], and up to 150 GHz [28], proving that LTCC technology offers cost-effective solutions also above 60 GHz. In this paper, an 8-element aperture coupled microstrip line-fed patch antenna (ACMPA) array is designed. The distance between the feed elements is designed for good beam-overlap that provides continuous coverage in H -plane direction. One SPDT and two SP4T switches are used to select the active feed element. The designed feed array is used to test the beam-steering properties of the 100-mm diameter optimized eccentricity Rexolite ($\epsilon_r = 2.53$) lens at 77 GHz.

The main reason for the choice of the lens type and material is to verify the result of [8]. Other important reasons are the mechanical simplicity and manufacturability of a single material lens with a canonical elliptical shape, low density, availability, and relatively low dielectric losses of Rexolite.

The design of the LTCC integrated feed array, switching network, and the lens are presented in Section 2. The beam-steering properties of the designed antenna are tested with radiation pattern measurements at 77 GHz in Section 3. The simulation and measurement results are used to study the beam-steering properties, i.e., scan loss, beam width, directivity, and cross-polarization as a function of the beam-steering angle. Also, the effects due to internal reflections and the origin of the side-lobes and cross-polarization are studied in detail.

2. BEAM-STEERING INTEGRATED LENS ANTENNA DESIGN

An integrated lens antenna consists of two parts: the dielectric lens and the feed array. The beam-steering principle with an integrated lens antenna is illustrated in Fig. 1. For electrical beam steering, a switching network is needed to select the active feed array element.

In this work, a LTCC integrated feed array with a switching network and a 100-mm diameter Rexolite lens are designed. The LTCC feed array is presented in Section 2.1. The aperture coupled microstrip line-fed patch feed elements radiation pattern into the lens is given in Section 2.2. It is used in the lens simulations in Sections 2.3 and 3.

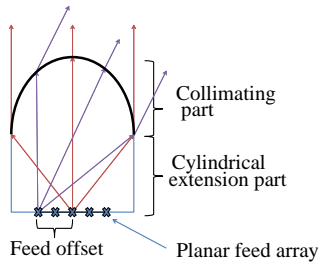


Figure 1. An illustration of the beam-steering principle with a rotationally symmetric dielectric lens antenna. Feed offset is defined as the feed elements distance from the rotational symmetry axis of the lens.

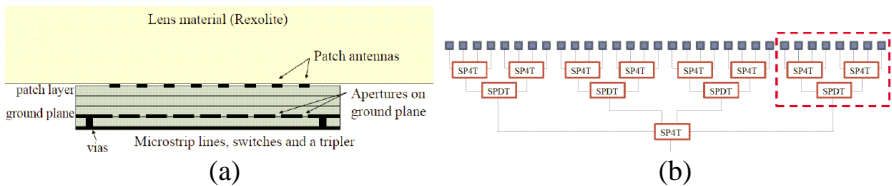


Figure 2. (a) LTCC layer structure (not in scale). The patch elements are on the top layer, the H-shaped apertures on the ground plane, and the switching network and the tripler are on the bottom layer. (b) A switching network for large one-dimensional beam-steering range; the realized 8-element sub array is outlined.

2.1. Integrated LTCC Feed Array and Switching Network

The array and switching network are designed for E-band. Ferro A6-M LTCC system is used with four 0.097 mm-thick tape layers with dielectric constant of $\epsilon_r = 5.7$ and $\tan \delta = 0.0015$ [21, 22]. The switching network is on the bottom surface, and the feed array patches on the top surface (Fig. 2). The antenna elements and the lens are separated from the active elements by a ground plane that effectively prevents any spurious radiation from the switching network into the lens.

The aperture coupled microstrip line-fed patch antenna elements are similar in construction to the one presented in [21, 22]. The patch and the H-shaped aperture are optimized to radiate into a half-space filled with the lens material ($\epsilon_r = 2.53$) at 77 GHz. The patch width is 0.66 mm and length 0.54 mm. Simulated single antenna element bandwidth is 68–91 GHz ($|\mathcal{S}_{11}| < -10$ dB) and peak gain is 6.7 dBi at

77 GHz. The patch antenna elements are arranged in a linear array in H -plane with a pitch of 2.0 mm. The simulated coupling to neighboring element is low ($|S_{21}| < -22$ dB). The distance between the elements is designed for beam overlap of about -2 dB with the designed lens.

A schematic of the switching network for large one-dimensional beam-steering is shown in Fig. 2(b)). In this work, only eight feed elements are realized in order to keep the switching network losses and cost relatively low. The switching network for the eight element sub-array has one SPDT-type PIN-diode switch (Hittite HMC-SDD112) that is used to select one of the two four-element sub-arrays. SP4T-type PIN-diode switches (TriQuint TGS4306-FC) are used to select the active element of the chosen sub-array. According to the datasheets, the SPDT switch has typical insertion loss of 2 dB and isolation of 30 dB, and the SP4T switches have typical insertion loss of 3 dB and isolation of 20 dB. Attenuation in the microstrip lines is in the order of 1.4 dB/cm. The combined attenuation in the 8-element switching network, i.e., the insertion losses of 2 dB and 3 dB and an average of about 1.5 cm of microstrip lines, is approximated to be in the order of 7 dB. With the integrated beam-steering lens antennas the number of beams, i.e., the number feed elements, is limited due to the increasing switching network losses. In future, low loss switches could be used, e.g., SP4T RF-MEMS with insertion loss of only about 1 dB at 75 GHz is reported in [29].

A frequency tripler (HMC-XTB110) is implemented in the LTCC board and an attached K-connector is used for the 25.67 GHz input signal. The MMIC devices are mounted using flip-chip and wire-bonding techniques. The bias currents for the PIN-diode switches are controlled with a board of rocker switches. The designed feed is manufactured in VTT. A photograph of the feed array is shown in Fig. 3.

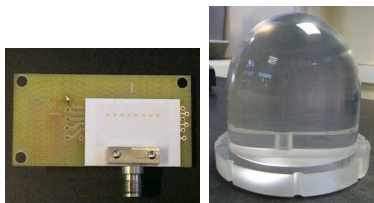


Figure 3. Photographs of the LTCC feed array attached to a circuit-board and the designed 100-mm diameter Rexolite lens. The total height of the lens equals 110.37 mm.

2.2. Feed Element Radiation Pattern into the Lens Material

The radiation pattern of a single aperture coupled microstrip lined patch antenna into Rexolite is simulated at 77 GHz using FDTD simulator developed by IETR [11, 30]. This radiation pattern is used in the ray-tracing simulations of the lens in Sections 2.3 and 3. The simulated amplitude and phase patterns are presented in Fig. 4. The simulated directivity into Rexolite half-space is 7.7 dB, and the half-power beam-widths are 66° and 91° in H -plane and E -plane, respectively. In general, the choice of directivity of the feed element

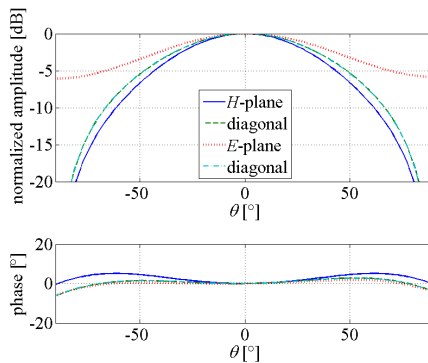


Figure 4. Simulated normalized main polarization amplitude and phase of the aperture coupled patch feed element into Rexolite ($\epsilon_r = 2.53$) half space at 77 GHz. The two diagonal planes are identical due to symmetry.

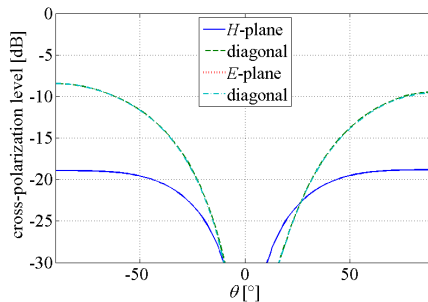


Figure 5. Simulated cross-polarization level of the aperture coupled patch feed element into Rexolite ($\epsilon_r = 2.53$) half space at 77 GHz. The two diagonal planes are identical due to symmetry. The simulated cross-polarization in the E -plane is below -50 dB.

is a compromise. With higher directivity feed elements, the reflection loss would be higher, and with lower directivity feed elements, the total of spillover and reflection losses are higher [7–9]. The simulated phase centre is about 0.15 mm below the patch, i.e., below the bottom of the lens. The phase centre is defined for minimal phase variations for $\theta < 30^\circ$. Its location is important as in the lens simulations the rays are launched from the phase centre point. With some feeds, as e.g., in [10], the phase centre can be quite far from the geometrical centre of the feed.

The simulated cross-polarization pattern is presented in Fig. 5. Ludwig's second definition of polarization [31] is used. The maximum cross-polarization level is about -9 dB.

2.3. Optimized Lens Shape

The conventional high directivity integrated lens types are the extended hemispherical [3–11] and the elliptical lens [6, 8, 12–18]. Diffraction-limited patterns are attained with an elliptical lens that has an eccentricity of $e = (\varepsilon_r)^{-1/2}$, and its extension length L equals $e \cdot a$, where ε_r is the relative permittivity of the lens material and a is the semimajor axis of the ellipse. The eccentricity of an ellipse is defined as

$$e = \sqrt{1 - (b/a)^2}, \quad (1)$$

where b is the semiminor axis of the ellipse, i.e., the radius of the lens. In the case of the hemispherical lens, the eccentricity is 0, and the diffraction-limited patterns can be approximated by optimizing the extension length [3–5, 7–11].

The mechanically simpler extended hemispherical lens is sometimes used to approximate the elliptical lens, e.g., [5, 6, 10, 16]. With high permittivity lenses, the beam-steering properties are relatively similar, e.g., in [6] with Alumina ($\varepsilon_r = 9.8$) and GaAs ($\varepsilon_r = 12.8$) lenses the difference in directivity is at most only about 1 dB. Similarly spherical reflector approximates paraboloidal reflector with large f/D compared to D/λ [32]. With low permittivity integrated lenses the difference is much larger both in mechanical dimensions and in beam-steering properties.

In [8], it is proposed for the first time that the eccentricity of low permittivity integrated lens can be optimized to improve the beam-steering properties. The role of the eccentricity on the focusing properties is studied with ray-tracing simulations using simple feed model and lossless lens material. The lens eccentricity is varied between 0 and $(\varepsilon_r)^{-1/2}$, the extension lengths are optimized for each eccentricity, and the beam-steering properties are studied based on

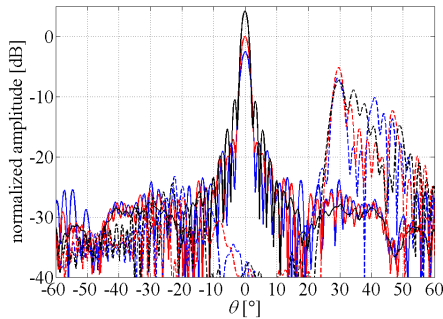


Figure 6. Normalized amplitude patterns simulated with FDTD with (dash) and without (solid) offsets at 77 GHz. Extended hemispherical lens (blue, offsets 0 and $270 = 40.50$ mm), optimized eccentricity lens (red, offsets 0 and $238\Delta = 35.70$ mm), and conventional elliptical lens (black, offsets 0 and $227\Delta = 34.05$ mm). The amplitudes are normalized to the maximum of the simulated on-axis beam of the optimized eccentricity lens.

simulations with feed offsets. The lens eccentricity and extension length optimization is presented in [8] and will not be repeated here. The optimal eccentricity of a low permittivity integrated lens for a beam-steering antenna is found to be an intermediate value between 0 and $(\epsilon_r)^{-1/2}$. Optimized eccentricity provides nearly constant beam width and directivity as a function of the beam-steering angle.

In this paper, the promising results from [8] are tested and analyzed with realized integrated feed array and lens. The geometrical parameters of the 100-mm-diameter optimized eccentricity Rexolite lens are chosen to be eccentricity of $0.78 \cdot (\epsilon_r)^{-1/2}$ and extension length of 53 mm [8]. A photograph of the lens is shown in Fig. 3.

The lens antenna is designed using an in-house developed ray-tracing program [3, 7, 8]. Because of the large electrical size of these high-directivity lenses ray tracing is preferred in antenna design and optimization compared to the computationally heavier full-wave simulations. Only the main result of [8], i.e., that the optimized eccentricity lens provides improved beam-steering properties with large offset, is confirmed with FDTD simulator developed by IETR [30]. In Fig. 6, the extended hemispherical lens ($e = 0$, $L = 70$ mm), the optimized eccentricity lens ($e = 0.78 \cdot (\epsilon_r)^{-1/2}$, $L = 53$ mm), and the conventional elliptical lens ($e = (\epsilon_r)^{-1/2}$, $L = e \cdot a \approx 40.4$ mm) are compared without offset and with 30° beam steering. The lenses have a diameter of 100 mm and the frequency is 77 GHz. In these

simulations the patch is only a simple square patch with a current element excitation, to make the simulation model simple, and therefore these results are not directly comparable with the results in Section 3. The FDTD cell size is $\Delta = 0.15$ mm and the feed is $4\Delta \times 4\Delta$ square patch with 2Δ -thick LTCC substrate and infinite ground plane. The optimized eccentricity lens has the smallest scan loss, i.e., decrease in amplitude compared to the on-axis beam, and highest amplitude and lowest side-lobes with the large offsets. Although the feed is not exactly the same as the realized LTCC feed, this result confirms the results of the lens eccentricity comparison of [8].

In [8], the feed radiation pattern is considered to be a point source with amplitude pattern

$$|\overline{E}(\phi, \theta)| = \cos^N(\theta), \quad 0 \leq \theta \leq 90^\circ, \quad 0 \leq \phi \leq 360^\circ, \quad (2)$$

at the main polarization of Ludwig's second definition of polarization [31]. The directivity of the feed element is varied with the parameter N . To confirm that the same conclusions about the role of the lens eccentricity can be made also with the realized aperture coupled patch feed antennas, the three lens shapes, the extended hemispherical, the optimized eccentricity, and the conventional elliptical, are compared with ray-tracing simulations. The simulated half-power beam-width, scan loss, directivity, and cross-polarization levels are presented in Figs. 12 and 13. Also, these results are then compared to the measurement results of the optimized eccentricity lens with the integrated feed array. Detailed analysis and comparison is presented

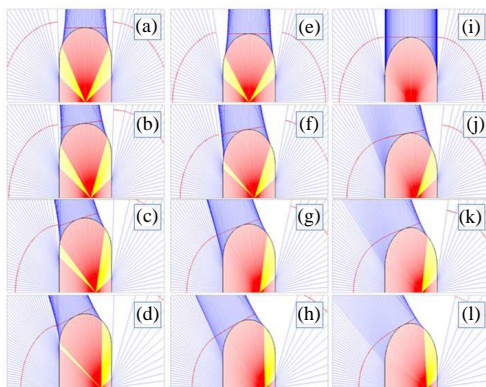


Figure 7. Ray illustrations; (a)–(d) extended hemispherical, (e)–(h) optimized eccentricity and (i)–(l) elliptical Rexolite lenses with feed offsets 0%, 20%, 40%, and 60% of the lens radius. Yellow rays are totally reflected. The red line outside the lens is an equiphase surface.

in Section 3.

In ray tracing different loss factors and field components can be easily separated and therefore ray tracing is an excellent tool for analyzing integrated lens antennas. In order to better understand the role of the lens eccentricity let us examine in detail Fig. 7, in which the extended hemispherical, the optimized eccentricity, and the elliptical Rexolite lenses are compared with and without feed offsets. Three observations can be made from Fig. 7:

1) A planar equiphase surface of variable diameter is formed by the hemispherical/elliptical part of the lens. The main-beam width, and therefore also directivity, depends mostly on the diameter of the planar section of the equiphase surface. In this paper, as also in [8], the equivalent currents are calculated on the equiphase surface (Fig. 7). The equiphase surface is orthogonal to the rays, and therefore tangential to integration surface, and thus, it is not necessary to approximate the tangential field by projection, as e.g., in [5, 10, 12, 15]. Comparison of using different integration surfaces is outside the scope of this paper.

2) Significant portion of the rays come out from the cylindrical part of the lens. The power leaking out from the extension is defined as the spillover loss

$$L_{spill} = 10 \cdot \log_{10}(P_{tot}/(P_{tot} - P_{spill})), \quad (3)$$

where P_{spill} is the total power leaking out from the extension part and P_{tot} the total power radiated by the feed into the lens. The spillover losses spread nearly equally in all directions, as can be seen from Fig. 7, and can have significant effects on side-lobe levels. The spillover loss depends on the feed element directivity and on the extension length [7–9].

3) Total reflections are shown with yellow rays. It can be seen that especially with feed offsets there is a large angular range of total reflections from the feed point of view. Therefore also with low permittivity lens materials there are strong internal reflections. However, the internal reflections are not taken into account in the simulated far-fields of the lens. Instead, the total power coupling to the internal reflections is calculated for each case and taken into account as reflection loss. The reflection loss is defined as

$$L_{refl} = 10 \cdot \log_{10}(P_{tot}/(P_{tot} - P_{refl})), \quad (4)$$

where P_{refl} is the total reflected power. The reflected fields could be calculated with ray tracing [15], but it multiplies the simulation time and computational complexity of otherwise simple and fast method. The internal reflections are known to affect the radiation pattern [9, 11, 12, 15, 16], input impedance of the feed [11, 15, 16], and

the mutual coupling [17]. In case of total reflections also a surface wave is generated that is partly responsible for the effects generally associated with internal reflections, i.e., with P_{refl} .

Because the reflection loss increases as a function of the feed offset it should be considered as one of the limiting factors for the maximum usable offset [5, 7, 12]. With large feed offsets, the reflection loss can be more than 3 dB (50%) with any feed element directivity and with any lens eccentricity or permittivity. This is due to the fact that, with large enough feed offset, there is total reflection directly above the feed (e.g., see Figs. 7(d), (h), and (l)), i.e., at the direction of the maximum of the feed radiation pattern. For example, with the optimized eccentricity Rexolite lens used in this paper, there is total reflection directly above the feed with offsets of 29 mm (58% of radius) or more. With feed offsets, the edge illumination is far from the optimal as defined in [18].

The imaginary part of permittivity is taken into account only as power loss and not in Snell’s law or reflection or transmission coefficients [33]. This approximation can be made because Rexolite is relatively low loss material ($\tan \delta = 0.0013$ in W-band [34]). Similar to spillover and reflection losses, the dielectric loss is calculated as

$$L_{diel} = 10 \cdot \log_{10}(P_{tot}/(P_{tot} - P_{diel})), \tag{5}$$

where P_{diel} is the power loss due to dielectric loss. Due to the fact that the reflected fields are not calculated in the simulations, Eq. (5) underestimates the total dielectric losses as the reflected fields are also attenuated due to dielectric losses before exiting the lens.

The simulated spillover, reflection, and dielectric losses, with the realized patch feed, of the extended hemispherical lens, the optimized eccentricity lens, and the conventional elliptical lens are compared in

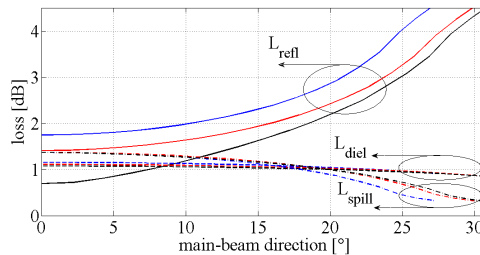


Figure 8. Simulated reflection (solid), spillover (dash-dot), and dielectric (dash) losses as a function of the main-beam direction with the simulated LTCC patch at 77 GHz. Extended hemispherical lens (blue), optimized eccentricity lens (red), and conventional elliptical lens (black).

Fig. 8. The spillover losses are nearly identical because the lenses are identical in the lens extension below the total reflection (Fig. 7). Also the dielectric losses are nearly equal because of the relatively small differences in the lens sizes. The reflection losses increase as a function of the main-beam direction with all the lens shapes mainly due to the total reflections. With small beam-steering angles the conventional elliptical lens has clearly the lowest reflection loss, but with large angles has nearly equal losses with the optimized eccentricity lens.

3. MEASUREMENT RESULTS

The radiation patterns are measured with the designed optimized eccentricity Rexolite lens and the LTCC patch antenna array at 77 GHz. The beam-steering properties of the lens are tested by switching the elements on one by one and measuring the radiation patterns.

The antenna is measured in a planar near-field scanning range with AB Millimetre MVNA 8-350 vector network analyzer as the measurement device. An external frequency doubler is used in order to provide the 25.67 GHz signal for the frequency tripler integrated in the LTCC board. Antenna gain measurements are not conducted as with the integrated feed it is difficult and time consuming, requiring additional test structures, and is considered to be beyond this study. A harmonic mixer is used as the receiver. An open-ended WR-10 waveguide is the probe antenna. Probe correction is done with the simulated radiation pattern obtained from FDTD simulator [30]. Most of the measurements are done with a relatively small scanning area (390 mm \times 390 mm) and with a sampling interval (3 mm) larger than the Nyquist sampling criterion ($\lambda_0/2$) in order to reduce the measurement time. In most cases, an angular range of $\pm 30^\circ$ is large enough. Some of the most important offsets are measured with a scanning area of 500 mm \times 500 mm and a scanning interval of 2 mm in order to capture a larger angular range of about $\pm 60^\circ$. The antenna measurements are done only at one frequency mainly to save time. According to simulations, frequency mainly affects the beam-width, as with diffraction limited beams the beam-width is directly proportional to wavelength.

As explained in Section 2, only an 8-element array is realized. In order to test larger beam-steering angles, the feed array is moved. First, the feed array is placed close to the centre of the lens so that the element 1 is at the centre and element 8 is at the feed offset of 14 mm. Then the whole feed array is moved manually, and feed offsets up to 36 mm are measured in order to test also the wide angle beam-steering

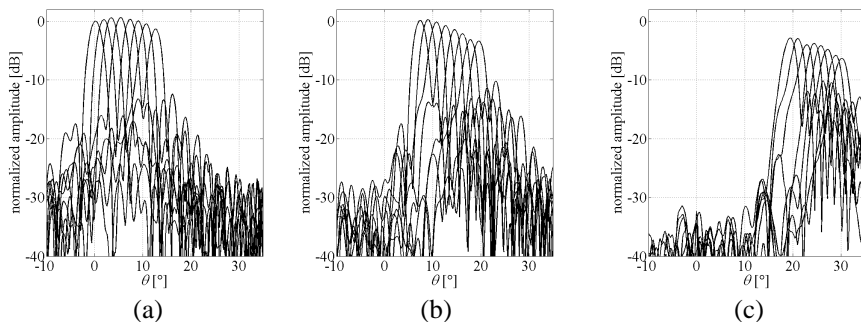


Figure 9. Measured normalized H -plane cuts with feed offsets from (a) 0 to 14 mm, (b) 8 mm to 22 mm, and (c) 22 mm to 36 mm. All patterns normalized to the maximum of the on-axis beam.

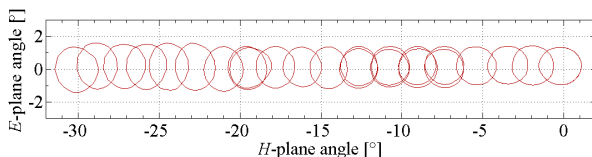


Figure 10. Measured -3 dB contours with feed offsets from 0 to 36 mm. The 3 dB contours illustrate only the angular range covered by each beam; the relative amplitudes are presented in Fig. 12(b).

properties. Patterns with feed offsets of 8 to 14 mm and 22 mm are measured twice. There are only small differences in the patterns and relative power levels (see Figs. 9, 10, 12, and 13) even though different patches and different switches were used. The measured normalized H -plane cuts at 77 GHz with feed offsets 0–36 mm are shown in Fig. 9. As expected, the main beam is steered nearly linearly as a function of the feed offset. A beam-steering range of about 13° is covered with the eight beams.

The beam overlap is between -1 dB and -2 dB over the whole beam-steering range. This beam overlap is well suitable for fine beam steering or tracking. The -3 dB contours of the measured patterns, shown in Fig. 10, provide a continuous one-dimensional coverage in H -plane direction.

The level of the first few side lobes is increasing as a function of the feed offset. Further away from the main beam, the side-lobe levels stay at around -25 dB to -30 dB. These side-lobe levels are partly due to fields from the hemielliptical part of the lens, partly due to fields

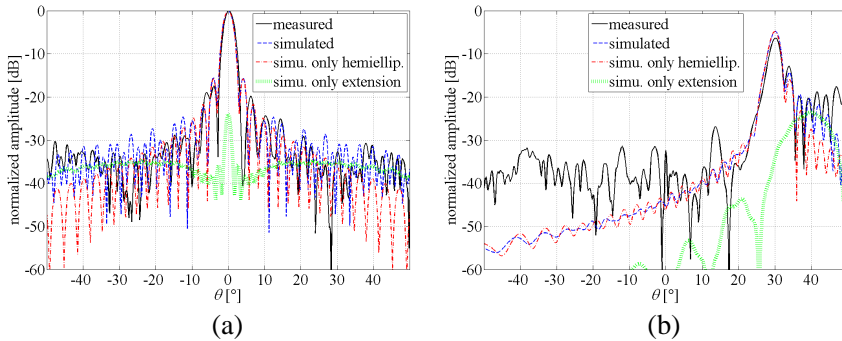


Figure 11. Measured and simulated normalized H -plane cuts (a) without feed offset and (b) with 36 mm feed offset. The internal reflections are not taken into account in the simulations. The measured amplitudes are normalized to the maximum of the measured on-axis beam. The simulated amplitudes are normalized to the maximum of the simulated on-axis beam.

leaking out from the cylindrical extension (spillover losses), and also partly due to reflected fields. This is better explained by examining Fig. 11, in which the measured and simulated normalized radiation patterns are presented with feed offsets 0 and 36 mm. In addition, the simulated patterns with the fields radiated by only the hemielliptical part or by only the cylindrical extension part are shown separately. These patterns are simulated, for diagnostic purposes, using the in-house developed ray-tracing program. Radiation patterns with all offsets are compared similarly (not shown for brevity). The difference between the measured and the simulated results can be assumed to be mostly due to reflected fields not included in the simulations. It can be seen that the main beam and the first side lobes originate from the hemiellipse. Side-lobe levels away from the main beam are strongly affected by the spillover losses. With large offsets, the reflection loss is very high and the reflected fields increase the side-lobe levels significantly. To our best knowledge, this kind of detailed explanation of the origin of side lobes has not been presented explicitly previously.

In Figs. 12 and 13, the measured half-power beam-widths (HPBW), main beam amplitudes, directivity, and cross-polarization are compared to the simulation results with ray tracing with the optimized eccentricity lens and also with the conventional lens shapes. The measured half-power beam-width in H -plane is $2.5^\circ \pm 0.2^\circ$ up to the largest measured beam-steering angle of 30° . The measured beam width is nearly constant and agrees well with the simulated beam width

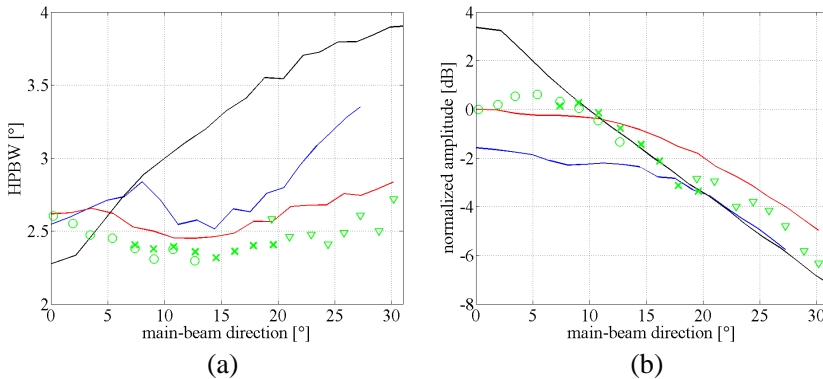


Figure 12. Measured (feed offsets from 0 to 14 mm (○), 8 mm to 22 mm (×), and 22 mm to 36 mm (▽)) and simulated (lines) *H*-plane half-power beam-widths (HPBW) and normalized amplitudes with feed offsets from 0 to 36 mm. The measured amplitudes are normalized to the maximum of the measured on-axis beam. The simulated amplitudes are normalized to the maximum of the simulated on-axis beam of the optimized eccentricity lens. The internal reflections are not taken into account in the simulations. Extended hemispherical lens (blue), optimized eccentricity lens (red), and conventional elliptical lens (black).

as a function of the main-beam direction as shown in Fig. 12(a)). With the extended hemispherical and with the conventional elliptical lenses the beam-width increases significantly with large beam-steering angles.

The measured normalized maximum main polarization amplitude decreases about 6 dB, from boresight to 30° (Fig. 12(b)). The simulated scan loss of about 5 dB agrees well with the measured one. The comparison of the simulated normalized amplitudes, with the different lens shapes, shows that the optimized eccentricity lens has the smallest scan loss and the highest amplitude with the large beam-steering angles.

The measured and simulated directivities are compared in Fig. 13(a). The measured directivities are calculated only from the large near-field scans (500 mm × 500 mm). The measured directivity decreases by about 2 dB from boresight to 20°–30° because of the increasing side-lobe levels (Figs. 9 and 13). Also, the simulated reflection loss increases as a function of the beam-steering angle (Fig. 8). Because the internal reflections are not taken into account in these simulations the ray-tracing simulations do not accurately

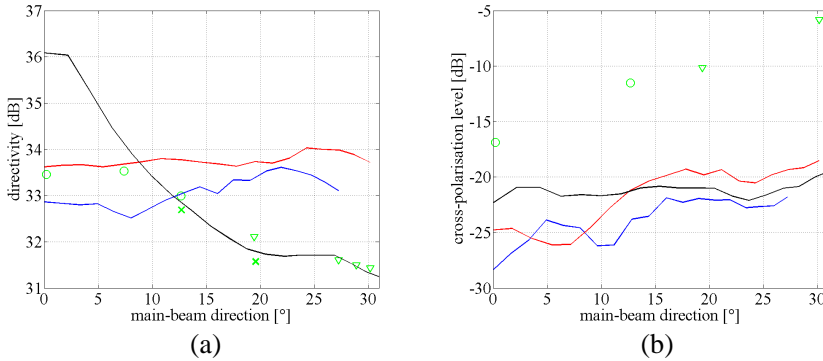


Figure 13. Measured (feed offsets from 0 to 14 mm (\circ), 8 mm to 22 mm (\times), and 22 mm to 36 mm (∇)) and simulated (lines) directivities and cross-polarization levels with feed offsets from 0 to 36 mm. Measured directivities are calculated only from the large near-field scans ($500 \text{ mm} \times 500 \text{ mm}$). The internal reflections are not taken into account in the simulations. Extended hemispherical lens (blue), optimized eccentricity lens (red), and conventional elliptical lens (black).

predict the realized directivity without considering also the increasing reflection loss. The optimized eccentricity lens has higher simulated directivity and lower reflection losses than the extended hemispherical lens. With small beam-steering angles (up to about 10° – 15°) the conventional elliptical lens has the highest amplitude and directivity, and the lowest losses. However, with large beam-steering angles the optimized eccentricity lens is better. It should be noted that also with the conventional elliptical lens or the hemispherical lens the reflection losses decrease the directivity as compared to the simulated directivities.

The cross-polarization patterns are measured with feed offsets 0 and 14 mm, and also after moving the feed array with larger feed offsets of 22 mm and 36 mm. For these measurements, the open-ended waveguide probe is turned 90° , and the larger scanning area of $500 \text{ mm} \times 500 \text{ mm}$ and the scanning interval of 2 mm are used. Ludwig's second definition of polarization [31] is used with the far-fields. In Fig. 13(b), the measured maximum cross-polarization levels are compared to the simulated cross-polarization levels. The cross-polarization of the feed is included in the simulations and, based on the simulation results, it is mainly responsible for the simulated cross-polarization. The measured cross-polarization levels are about 10 dB higher than the simulated.

This difference is probably due to the internal reflections. Inside the -3 dB contours of the main beam the measured and the simulated cross-polarization levels are within ± 2 dB from each other. The high measured levels of cross-polarization are outside the main beam.

4. CONCLUSION

An integrated lens antenna is designed and electrical beam steering is demonstrated at 77 GHz. An 8-element aperture coupled patch antenna feed array with a switching network is integrated in LTCC. One SPDT and two SP4T PIN-diode switches are used to select the active element. The feed array is integrated to the bottom of a 100-mm diameter Rexolite lens. The eccentricity of the lens is optimized with ray-tracing simulations for improved beam-steering properties. The ray-tracing result is verified with full-wave FDTD simulations. The designed optimized eccentricity lens is compared with simulations to the conventional extended hemispherical and elliptical lenses.

The designed antenna is tested with radiation pattern measurements using planar near-field scanning. The eight elements are arranged in a linear configuration with a pitch of 2 mm, and they provide a continuous coverage in H -plane with beam overlap of -1 dB to -2 dB between adjacent beams. Beam-steering range of about 13° is covered with the eight beams. Also the wide angle beam-steering properties are tested, by manually moving the whole feed array, and beam-steering angles up to 30° are tested. The effects due to the reflection and the spillover losses are analyzed in detail using both the ray-tracing simulation and the measurement results. Side-lobe levels away from the main beam are strongly affected by the spillover losses. Because of the internal reflections the side-lobes and cross-polarization outside the main-beam region increase compared to the simulation results. These results highlight that the lens shape can be optimized with the simple and fast ray-tracing simulations when the reflection losses are also taken into account in the comparison of different lens shapes.

The measured directivity decreases by about 2 dB from the boresight up to 20° – 30° beam-steering angles due to the increasing reflection losses. The measured scan loss from boresight to 30° is about 6 dB. The optimized eccentricity lens results in smaller scan loss than the conventional low permittivity lenses. The half-power beam-width in H -plane is $2.5^\circ \pm 0.2^\circ$ up to the largest measured beam-steering angle. Good scanning characteristics are obtained with the designed lens for a very wide angular range of $\pm 30^\circ$.

ACKNOWLEDGMENT

This work was supported in part by the Academy of Finland through the Centre of Excellence program (SMARAD), and Tekes through BRAWE and BEAMS projects. The authors would like to thank VTT's LTCC-processing staff, Mr. E. Kahra for his help in mechanical work, and Dr. N. T. Nguyen for his help with the FDTD simulations.

REFERENCES

1. Rasshofer, R. R. and K. Naab, "77 GHz long range radar systems status, ongoing developments and future challenges," *Proc. 2nd Eur. Radar Conf.*, 161–164, Paris, France, 2005.
2. ETSI-Standard, ETSI EN 302 217-4-2 v1.4.1 (2008-8), Fixed Radio Systems; Characteristics and requirements for point-to-point equipment and antennas; Part 4–2: Antennas, 36, 2008.
3. Ala-Laurinaho, J., A. Karttunen, J. Säily, A. Lamminen, R. Sauleau, and A. V. Räsänen, "Mm-wave lens antenna with an integrated LTCC feed array for beam steering," *Proc. 4th Eur. Conf. Antennas Propag.*, C09P1-2/1841151, Barcelona, Spain, Apr. 12–16, 2010.
4. Artemenko, A., A. Maltsev, R. Maslennikov, A. Sevastyanov, and V. Ssorin, "Beam steerable quartz integrated lens antenna for 60 GHz frequency band," *Proc. 5th Eur. Conf. Antennas Propag.*, 788–792, Rome, Italy, Apr. 11–15, 2011.
5. Filipovic, D. F., G. P. Gauthier, S. Raman, and G. M. Rebeiz, "Off-axis properties of silicon and quartz dielectric lens antennas," *IEEE Trans. Antennas Propag.*, Vol. 45, No. 5, 760–766, May 1997.
6. Van der Vorst, M. J. M., P. J. I. de Maagt, and M. H. A. J. Herben, "Scan-optimized integrated lens antennas," *Proc. 27th European Microwave Conference*, 605–610, Jerusalem, Israel, 1997.
7. Karttunen, A., J. Ala-Laurinaho, R. Sauleau, and A. V. Räsänen, "A study of extended hemispherical lenses for a high-gain beam-steering antenna," *Proc. 4th Eur. Conf. Antennas Propag.*, A25-1/1842008, Barcelona, Spain, Apr. 12–16, 2010.
8. Karttunen, A., J. Ala-Laurinaho, R. Sauleau, and A. V. Räsänen, "Optimal eccentricity of a low permittivity integrated lens for a high-gain beam-steering antenna," *Proc. 5th Eur. Conf. Antennas Propag.*, 3522–3526, Rome, Italy, Apr. 11–15, 2011.
9. Karttunen, A., J. Ala-Laurinaho, R. Sauleau, and A. V. Räsänen, "Reduction of internal reflections in low permittivity integrated

- lens antennas,” *Proc. Millimetre Wave Days*, Espoo, Finland, May 23–25, 2011.
10. Lombart, N., G. Chattopadhyay, A. Skalare, and I. Mehdi, “Novel terahertz antenna based on a silicon lens fed by a leaky wave enhanced waveguide,” *IEEE Trans. Antennas Propag.*, Vol. 59, No. 6, 2160–2168, Jun. 2011.
 11. Godi, G., R. Sauleau, and D. Thouroude, “Performance of reduced size substrate lens antennas for millimeter-wave communications,” *IEEE Trans. Antennas Propag.*, Vol. 53, No. 4, 1278–1286, Apr. 2005.
 12. Wu, X., G. V. Eleftheriades, and T. E. van Deventer-Perkins, “Design and characterization of single- and multiple-beam mm-wave circularly polarized substrate lens antennas for wireless communications,” *IEEE Trans. Microwave Theory Tech.*, Vol. 49, No. 3, 431–441, Mar. 2001.
 13. Boriskin, A. V. and R. Sauleau, “Synthesis of arbitrary-shaped lens antennas for beam-switching applications,” *Proc. 40th European Microwave Conference*, 739–742, Paris, France, Sept. 28–30, 2010.
 14. Boriskin, A. V. and R. Sauleau, “Lens shaping aimed at improvement of the beam-switching antenna off-axis properties,” *Proc. 2nd Eur. Conf. Antennas Propag.*, 739–742, Edinburgh, UK, Nov. 11–16, 2007.
 15. Van der Vorst, M. J. M., P. J. I. de Maagt, and M. H. A. J. Herben, “Effect of internal reflections on the radiation properties and input admittance of integrated lens antennas,” *IEEE Trans. Microwave Theory Tech.*, Vol. 47, No. 9, 1696–1704, Sept. 1999.
 16. Van der Vorst, M. J. M., P. J. I. de Maagt, A. Neto, A. L. Ryenolds, R. M. Heeres, W. Luinge, and M. H. A. J. Herben, “Effect of internal reflections on the radiation properties and input admittance of integrated lens antennas comparison between measurements and theory,” *IEEE Trans. Microwave Theory Tech.*, Vol. 49, No. 6, 1118–1125, Jun. 2001.
 17. Neto, A., A. Toccafondi, and S. Maci, “Mutual coupling between slots printed at the back of elliptical dielectric lenses,” *IEEE Trans. Microwave Theory Tech.*, Vol. 49, No. 6, 1118–1125, Jun. 2001.
 18. Boriskin, A. V., R. Sauleau, and A. I. Nosich, “Performance of hemielliptic dielectric lens antennas with optimal edge illumination,” *IEEE Trans. Antennas Propag.*, Vol. 57, No. 7, 2193–2198, Jul. 2009.
 19. Costa, J. R., M. Silveirinha, and C. A. Fernandes, “Double-shell

- axial-symmetric imaging lens antenna for space applications,” *Antennas and Propagation Society International Symposium*, Vol. 1B, 438–441, Jul. 2005.
20. Costa, J. R., M. G. Silveirinha, and C. A. Fernandes, “Evaluation of a double-shell integrated scanning lens antenna,” *IEEE Antennas Wireless Propag. Lett.*, Vol. 8, 781–784, Oct. 2008.
 21. Lamminen, A., J. Säily, and A. Vimpari, “Design and processing of 60 GHz antennas on low temperature co-fired ceramic (LTCC) substrates,” *Proc. 4th ESA Workshop on Millimetre-Wave Technology and Applications*, 43–48, Espoo, Finland, Feb. 15–17, 2006.
 22. Lamminen, A. E. I., J. Säily, and A. R. Vimpari, “60-GHz patch antennas and arrays on LTCC with embedded-cavity substrates,” *IEEE Trans. Antennas Propag.*, Vol. 56, No. 9, 2865–2874, Sept. 2008.
 23. Pursula, P., T. Karttaavi, M. Kantanen, A. Lamminen, J. Holmberg, M. Lahdes, I. Marttila, M. Lahti, A. Luukanen, and T. Vähä-Heikkilä, “60-GHz millimeter-wave identification reader on 90-nm CMOS and LTCC,” *IEEE Trans. Microwave Theory Tech.*, Vol. 59, No. 4, 1166–1172, Apr. 2011.
 24. Kam, D., D. Liu, A. Natarajan, S. Reynolds, H.-C. Chen, and B. A. Floyd, “LTCC packages with embedded phased-array antennas for 60 GHz communications,” *IEEE Microwave and Wireless Components Letters*, Vol. 21, No. 3, 142–144, Mar. 2011.
 25. Niciloiu, D., M. Lahti, A. Stefanescu, A. A. Muller, and T. Vähä-Heikkilä, “Design and experiments of 77 GHz antennas in LTCC technology,” *Proc. 5th Eur. Conf. Antennas Propag.*, 253–257, Rome, Italy, Apr. 11–15, 2011.
 26. Lamminen, A. and J. Säily, “Wideband stacked patch antenna array on LTCC for W-band,” *Proc. 5th Eur. Conf. Antennas Propag.*, 2962–2966, Rome, Italy, Apr. 11–15, 2011.
 27. Aguirre, J., H.-Y. Pao, H.-S. Lin, P. Garland, D. O’Neil, and K. Horton, “An LTCC 94 GHz antenna array,” *IEEE Antennas and Propagation Society International Symposium*, San Diego, CA, Jul. 2008.
 28. Khalil, A., D. Passerieux, S. Verdeyme, L. Rigaudeau, and D. Baillargeat, “150 GHz bandpass filter using LTCC technology,” *IEEE Microwave and Wireless Components Letters*, Vol. 19, No. 7, 455–457, Jul. 2009.
 29. Gong, S., H. Shen, and N. S. Baker, “A 60-GHz 2-bit switched-line phase shifter using SP4T RF-MEMS switches,” *IEEE Trans. Microwave Theory Tech.*, Vol. 59, No. 4, 894–900, Apr. 2011.

30. Hoteit, H., R. Sauleau, B. Philippe, P. Coquet, and J.-P. Daniel, "Vector and parallel implementations for the FDTD analysis of millimeter wave planar antennas," *Int. Journ. of High Speed Computing*, Vol. 10, No. 2, 209–234, Dec. 1999.
31. Ludwig, A. C., "The definition of cross polarization," *IEEE Trans. Antennas Propag.*, Vol. 21, No. 1, 116–119, Jan. 1973.
32. Holt, F. S. and E. L. Bouche, "A Gregorian corrector for spherical reflector," *IEEE Trans. Antennas Propag.*, Vol. 12, No. 1, 44–47, Jan. 1964.
33. Bourreau, D., A. Péden, and S. Le Maguer, "A quasi-optical free-space measurement setup without time-domain gating for material characterization in the W-band," *IEEE Trans. Instrum. Meas.*, Vol. 55, No. 6, 2022–2028, Dec. 2006.
34. Chang, P. C. Y., J. G. Walker, and K. I. Hopcraft, "Ray tracing in absorbing media," *Journal of Quantitative Spectroscopy & Radiative Transfer*, Vol. 96, 323–341, 2005.